Convectively Generated Internal Gravity Waves in the Lower Atmosphere of Venus. Part II: Mean Wind Shear and Wave–Mean Flow Interaction

R. DAVID BAKER* AND GERALD SCHUBERT+

Department of Earth and Space Sciences, University of California, Los Angeles, Los Angeles, California

PHILIP W. JONES

Theoretical Division, Los Alamos National Laboratory, Los Alamos, New Mexico

(Manuscript received 29 July 1998, in final form 10 March 1999)

ABSTRACT

This paper is the second of a two-part study that numerically investigates internal gravity wave generation by convection in the lower atmosphere of Venus. Part I of this study considers gravity wave generation and propagation in the absence of mean wind shear. In Part II, the Venus westward superrotation is included, and wave–mean flow interaction is assessed.

Both lower-atmosphere convection and cloud-level convection play active roles in the dynamics of the stable layer from 31- to 47-km altitude when mean wind shear is present. This result contrasts with the simulation without mean wind shear presented in Part I where cloud-level convection was primarily responsible for gravity wave generation in the stable layer. In the presence of mean wind shear, upward entrainment from lower-atmosphere convection and downward penetration from cloud-level convection are comparable in magnitude. Convectively generated internal gravity waves have horizontal wavelengths (~25–30 km) comparable to horizontal scales in both convection layers. Quasi-stationary gravity waves (with respect to the lower convection layer) occur in the lower part of the stable layer, while both eastward- and westward-propagating waves generated by cloud-level convection exist in the upper part of the stable layer. Simulated wave amplitudes and vertical wavelengths agree well with observations. Eastward-propagating waves generated by cloud-level convection experience critical level absorption in the stable layer and thus *decelerate* the Venus westward superrotation below the clouds. The deceleration is comparable in magnitude to zonal accelerations above the clouds by thermal tides.

1. Introduction

Evidence of waves within the stable layer in Venus's atmosphere from roughly 31- to 47-km altitude is abundant (Seiff et al. 1980; Counselman et al. 1980; Kerzhanovich and Marov 1983; Seiff et al. 1992; Jenkins et al. 1994; Hinson and Jenkins 1995). These waves are likely generated by convection given the close proximity of convection to the stable layer (lower-atmosphere convection occurs from roughly 18- to 30-km altitude and cloud-level convection occurs from roughly 48- to 55-km altitude) (Seiff et al. 1980). Part I of this study [Baker et al. (2000); hereafter referred to as P1] is a numerical investigation of internal gravity wave generation by convection in the absence of mean wind shear. In a shear-free environment, internal gravity waves in the stable layer are primarily generated by cloud-level convection with intrinsic horizontal phase speeds comparable to cloud-level downdraft velocities. Horizontal wavelengths are similar to dominant horizontal wavelengths in the cloud-level penetrative region. Entrainment by lower-atmosphere convection is weak compared to cloud-level penetration, and thus coupling between the lower convection layer and the overlying stable layer is minimal. Simulated wave amplitudes and vertical wavelengths agree well with observations, suggesting that cloud-level penetrative convection, in the absence of mean wind shear, may be responsible for wave features observed in the underlying stable layer.

The presence of mean wind shear can affect these results in two ways. First, wind shear introduces a second type of wave generation by convection. In the absence of mean wind shear, convection generates internal

* Current affiliation: NASA Goddard Space Flight Center, Universities Space Research Association, Greenbelt, Maryland.

+ Additional affiliation: Institute of Geophysics and Planetary Physics, University of California, Los Angeles, Los Angeles, California.

Corresponding author address: Dr. R. David Baker, NASA Goddard Space Flight Center, Code 912, Universities Space Research Association, Greenbelt, MD 20771.
E-mail: rbaker@agnes.gsfc.nasa.gov

gravity waves through the ''mechanical oscillator'' effect (Clark et al. 1986; Fovell et al. 1992). Downdrafts impinging on the underlying stable layer displace stable air vertically and thus excite internal gravity waves. Wind shear produces a second wave generation mechanism called the ''obstacle'' effect (Mason and Sykes 1982; Clark et al. 1986). Convective plumes that penetrate into an adjacent stable layer may act as temporary ''mountains'' and deflect horizontally traveling air parcels vertically. Gravity waves generated by the mechanical oscillator effect are characterized by relatively high frequencies and short wavelengths, whereas gravity waves generated by the obstacle effect are quasi-stationary, longer wavelength features (Fovell et al. 1992).

Second, in the presence of mean wind shear, vertically propagating gravity waves can interact with the mean circulation and modify the mean flow through critical level absorption. Linear, nondissipative internal gravity waves do not exchange momentum or energy unless they encounter a critical level, a level in which the phase speed of the wave matches the mean wind speed (Eliassen and Palm 1961). At a critical level, the wave group velocity becomes horizontal in direction such that wave energy cannot continue to propagate vertically. Instead, gravity wave momentum and energy become absorbed into the mean flow (Booker and Bretherton 1967; Lindzen 1990). Critical level absorption of convectively generated internal gravity waves has been proposed to explain the quasi-biennial oscillation in Earth's equatorial stratosphere (Holton and Lindzen 1972; Alexander and Holton 1997).

The atmosphere of Venus experiences westward zonal flow at all altitudes, ranging from a few meters per second in the lowest 10 km to roughly 100 m s^{-1} at 65-km altitude (Schubert 1983). The presence of large westward atmospheric wind velocities is commonly referred to as the Venus atmospheric superrotation; the solid planet rotates retrograde (from east to west) with a rotation period of 243 days, while the cloud-top atmosphere rotates in a retrograde fashion once every 4 days. Among the mechanisms proposed to explain the Venus westward superrotation is critical level absorption of vertically propagating gravity waves [Hou and Farrell (1987); see Schubert (1983) and Gierasch et al. (1997) for reviewed discussions of the maintenance of the Venus westward superrotation]. Hou and Farrell (1987) suggest that internal gravity waves, perhaps generated by convection near the surface, could transport a sufficient amount of westward momentum to maintain the superrotation below 45-km altitude. Above 45-km altitude, mechanisms other than critical level absorption, such as Hadley circulation redistribution of momentum (Gierasch 1975; Del Genio et al. 1993; Del Genio and Zhou 1996) or atmospheric tides (Newman and Leovy 1992), are required to support the Venus superrotation.

Recent results for cloud-level wave generation indicate that internal gravity waves do not significantly contribute to the Venus atmospheric superrotation *above* the clouds (Leroy and Ingersoll 1995). Gravity waves generated by convection in this model have intrinsic phase speeds (relative to the zonal wind within the convection layer) of 3–5 m s^{-1}. Because of the slow horizontal phase speeds, westward-propagating waves soon reach critical levels and dump their momentum and energy just above the convection layer at ~56-km altitude. Wave breaking also occurs in this region because a significant fraction of the wave fluctuations are convectively unstable upon emission. Since the westward waves propagate vertically only a short distance, wave amplitudes remain small and the net westward acceleration due to gravity waves is negligible.

In this paper, we investigate convectively generated internal gravity waves in the lower atmosphere of Venus in the presence of mean wind shear (the Venus westward superrotation). The vertical domain extends from 12- to 60-km altitude, thus including both the lower convection region and the cloud-level convection layer (Seiff et al. 1980). The gravity waves of interest occur in the stable layer from 31- to 47-km altitude, bounded above and below by convection layers. Characteristics of convectively generated internal gravity waves in the model are determined and compared with observations, and wave–mean flow interaction is assessed. The next section describes the model, and section 3 presents results of the simulation. The implications of these results for Venus's atmosphere are discussed in the final section.

2. Model

The mathematical model of Venus's atmosphere and the numerical approach are described in P1. A two-dimensional, nonlinear, fully compressible model of a perfect gas is used to simulate Venus's atmospheric convection and gravity wave generation (Baker et al. 1998, 1999, 2000). The model setup for the simulation presented here is identical to that presented in P1 except that the Venus westward superrotation is included. Specific parameter values are listed in Table 1 of P1. Venus-like background thermal and mean wind profiles similar to those used by Young et al. (1987) are adopted (Fig. 1). A Galilean transformation of the background mean wind has been performed such that the mean wind is zero in the cloud-level convection layer. The simulation considers solar heating at the subsolar point. Small-scale turbulence is modeled by eddy diffusion with constant diffusion coefficients. The effective Rayleigh numbers (a measure of the degree of thermal instability in a fluid, defined in P1) for the lower convection layer and for the cloud-level convection layer are 1.2×10^6 and 6.8×10^6, respectively.

The computational domain extends 120 km horizontally and spans vertically from 12- to 60-km altitude. A grid of 850×403 points with a horizontal grid spacing of ~0.14 km and a vertical grid spacing of ~0.12 km is used. The horizontal resolution is slightly higher than in P1 to prevent small-scale numerical instabilities as-

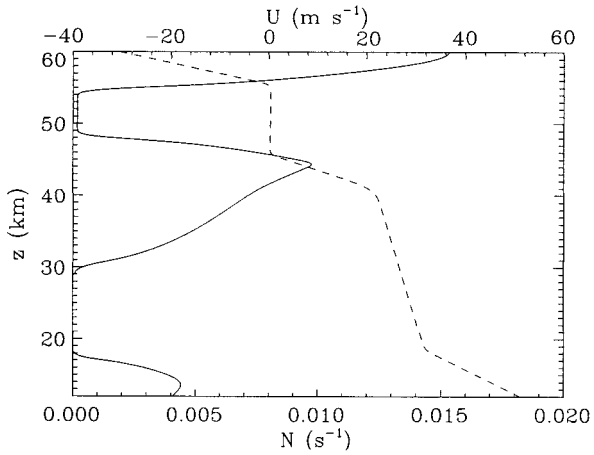

FIG. 1. Brunt–Väisälä frequency N (solid) and mean wind U (dashed) of the background state as a function of altitude z.

sociated with sheared convective features in the cloud-level penetrative region. A small time step of approximately 0.088 *s* is required to meet the Courant condition for stability. The horizontal boundaries are stress-free with a fixed heat flux and the side boundaries are periodic. The value of heat flux at the boundaries is equal to but opposite in sign from the solar flux at that level. The initial condition for the mean wind shear case is the final solution of the no wind shear case from P1. Short transient phases occur as the simulation adjusts from the initial condition to a statistically steady state in the convection layers (the stable layers do not reach a statistically steady state due to wave–mean flow interaction). The statistically steady integration time is 33.1 simulation hours.

3. Results

a. Convection characteristics

Mean wind shear affects the characteristics of convection and gravity waves in Venus's atmosphere. Figure 2 shows residual potential temperature θ'' (total potential temperature minus the horizontally averaged potential temperature) and the velocity field for the simulation with mean wind shear at two instances in time as a function of horizontal distance x and altitude z. Cold, narrow downwellings occur in the cloud-level convection layer but not as regularly spaced coherent structures as in the calculation without mean wind shear (cf. P1, Fig. 4). For example, a cold, narrow downdraft can be seen in Fig. 2a near $x = 83$ km, $z = 54$ km. However, a more diffuse collection of cool air can be seen from roughly $x = 0$ km to $x = 30$ km in the cloud-level convection layer. This region consists of both updrafts and downdrafts with moderate velocities of ~3–8 m s^{-1}. A stronger downdraft occurs at the edge of this cool air near $x = 5$ km, $z = 54$ km with a downward velocity of ~13 m s^{-1}. As in the case with no mean wind shear (hereafter called the shear-free case), typical convective downdraft velocities (~9–13 m s^{-1}) are larger than typical upflow velocities (~3–58 m s^{-1}). However, unlike in the shear-free simulation, large upward velocities do occasionally occur in the cloud-level convection layer in the presence of mean wind shear (e.g., large upward velocities are present within the upflow plume located at $x = 118$ km, $z = 50$ km in Fig. 2a). The maximum upward velocity (14.5 m s^{-1}) in the mean wind shear case is comparable in magnitude to the maximum downward velocity (−15.1 m s^{-1}). In general, features in the cloud-level penetrative region have larger horizontal wavelengths (~30 km) in the case with mean shear than in the shear-free case (~15 km).

Large amplitude gravity waves ($\theta'' \approx 1.5$ K) are generated in the overlying stable layer from roughly 56- to 60-km altitude by convective penetration and entrainment (Fig. 2). These gravity waves are revealed by large warm and cold patches at the top of the domain. They are artificially ducted by the upper boundary at 60 km, so gravity wave characteristics from 56- to 60-km altitude in our simulations cannot be directly related to features in Venus's atmosphere. Strong downward penetration also occurs in the case with mean wind shear, and penetrative compressional features again can be seen near 45-km altitude. The number of strong compressional features shown in Fig. 2a is uncharacteristically small; twice as many compressional features occur at later times (Fig. 2b). Internal gravity waves in the stable layer from 31- to 47-km altitude occur with larger horizontal scales (wavelengths ~25–35 km) than in the shear-free case (~10–15 km). Characteristics of internal gravity waves will be discussed in more detail below.

Lower-atmosphere convection is also significantly modified by the mean wind. Convective structure is complex in the lower atmosphere; both relatively warm upwellings and relatively cold upflows occur next to each other (e.g., $x = 60$ km, $z = 20$ km in Fig. 2a). Indeed, the cold feature at $x = 65$ km, $z = 20$ km in Fig. 2a is reminiscent of cold-pool gust fronts in thunderstorms on Earth (Droegemeier and Wilhelmson 1987). Although evaporative cooling is instrumental in cold pool formation on Earth but is a relatively unimportant process on Venus (Knollenburg and Hunten 1980), the similarity between cold pools on Earth and in our simulation is unmistakable. The cold pool is associated with relatively strong inflow, and strong convergence and uplift occur at the cold pool boundary. The lower boundary at 12-km altitude possibly influences the vertical location of the cold pool in our simulation (convective penetration is limited by the lower boundary as discussed below). However, atmospheric static stability (Fig. 1) is probably a larger factor in the determination of cold pool altitudes. Both relatively warm downflows ($x = 25$ km, $z = 30$ km) and relatively cold downdrafts ($x = 100$ km, $z = 30$ km) are also present in the lower convection layer. Typical updraft

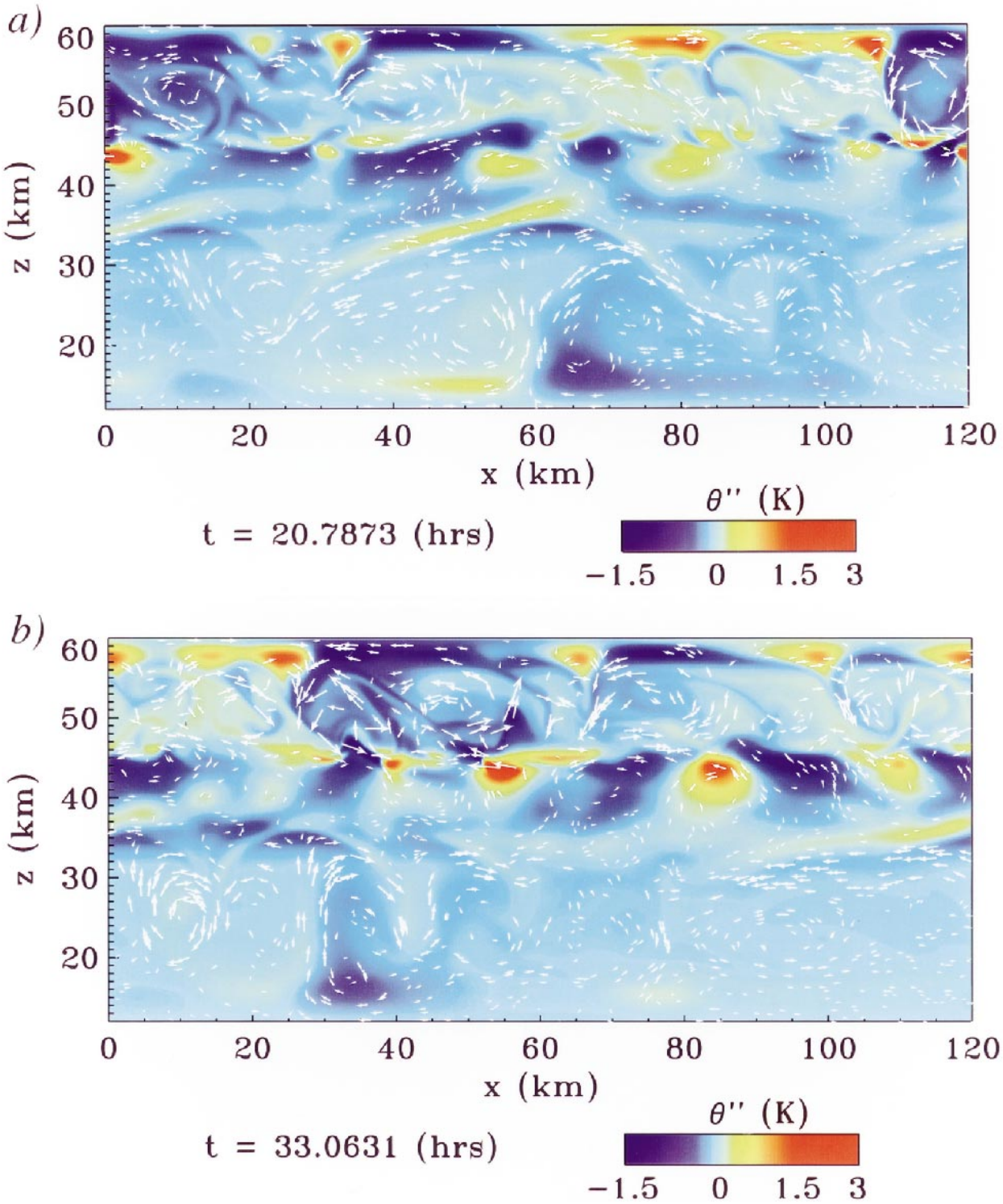

FIG. 2. Residual potential temperature θ'' (colors) and velocity field (arrows) at (a) t = 20.7873 h and (b) t = 33.0631 h. The lower convection layer spans from 17- to 31-km altitude, and the cloud-level convection layer extends from 47- to 56-km altitude. Stable layers occur from 12- to 17-km altitude, 31- to 47-km altitude, and 56- to 60-km altitude. The longest arrow represents a velocity of 15.1 m s^{-1}.

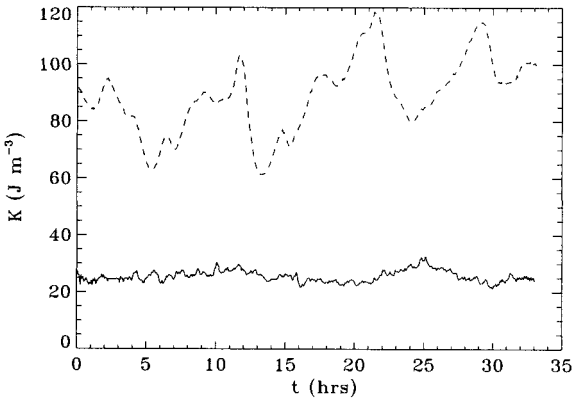

FIG. 3. Spatially averaged deviation kinetic energy density K' for the cloud-level convection layer (solid) and the lower convection layer (dashed) as a function of time.

and downdraft velocities are comparable in magnitude (~4–8 m s^{-1}), slightly larger than in the shear-free calculation. The complex behavior of lower-atmosphere convection occurs throughout the simulation. Cold pools of air near the bottom of the layer and both warm and cool downdrafts are also present later in the simulation (Fig. 2b).

Figure 3 plots the time series of spatially averaged deviation kinetic energy density K' for the lower convection layer and the cloud-level convection layer. Here, K' is defined as the kinetic energy density within the convection layer due to velocity deviations from the background mean wind profile:

$$K' = \left\langle\left\langle \frac{1}{2}\rho u_i' u_i' \right\rangle\right\rangle, \tag{1}$$

where ρ is density, u_i is velocity in the x_i direction, and primes denote deviations from the background state. Double angle brackets indicate spatial averaging (both horizontally and vertically). Time-averaged values of K' are two to three times larger in the mean wind shear case than in the shear-free case (cf. P1, Fig. 5) because velocity deviations from the background state are larger due to convection–mean flow interaction (discussed in more detail in section 3c below). Flows in both convection layers are time dependent (Fig. 3). Spectral analysis of K' in the lower convection layer reveals dominant periods of approximately 11 h, 3 h, and 90 min (Fig. 4), slightly longer than the dominant periods of the lower convection layer in the shear-free case. Although mean wind shear modifies the convective planform in the lower convection layer, the characteristic timescales are only slightly modified. Cloud-level convection experiences dominant periods of roughly 14 h, 2 h, 90 min, 60 min, 20 min, and 10 min. Both the long timescale modulation of 14 h and the short timescale oscillations of less than 30 min do not appear in the kinetic energy density time series for the shear-free case (P1, Fig. 6). Thus, addition of mean wind shear produces

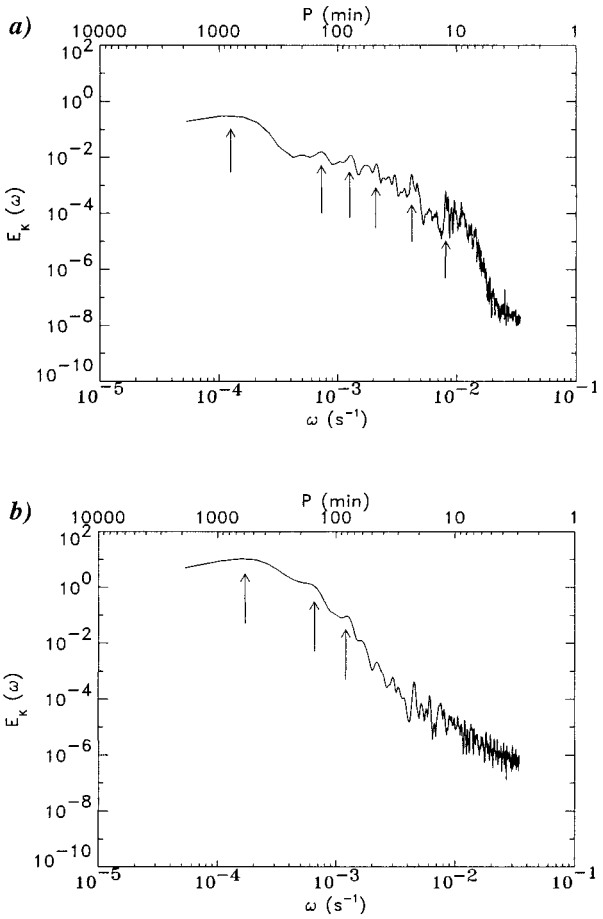

FIG. 4. Power spectral density E_K of spatially averaged deviation kinetic energy density K' as a function of angular frequency ω and period P for the cloud-level convection layer (top) and the lower convection layer (bottom). Arrows indicate dominant peaks discussed in the text. The units of E_K are J^2 m^6 s^{-1}.

both low and high frequency fluctuations in the cloud-level convection layer.

Horizontal length scales of convection in the simulation with a Venus-like mean wind (Fig. 5) are slightly larger than horizontal scales in the shear-free case (P1, Fig. 7). In Fig. 5, horizontal spectra of density-weighted vertical velocity $\rho^{1/2}w'$ are taken at each altitude and then temporally averaged from $t = 17.7$ h to $t = 33.1$ h at time intervals of roughly 70 min. Cloud-level convection experiences a dominant wavelength of ~30 km in the middle of the layer and a slightly broader range of wavelengths (~10–30 km) near the bottom. These scales are comparable to horizontal scales of cloud-level convection found in the simulation without mean wind shear. Lower-atmosphere convection scales are slightly larger in the case with mean wind shear (~25–50 km) compared to the case without mean wind shear (~20–30 km). Similarly, internal gravity waves in the stable layer from 31- to 47-km altitude exhibit longer dominant wavelengths in the presence of mean wind shear (wave-

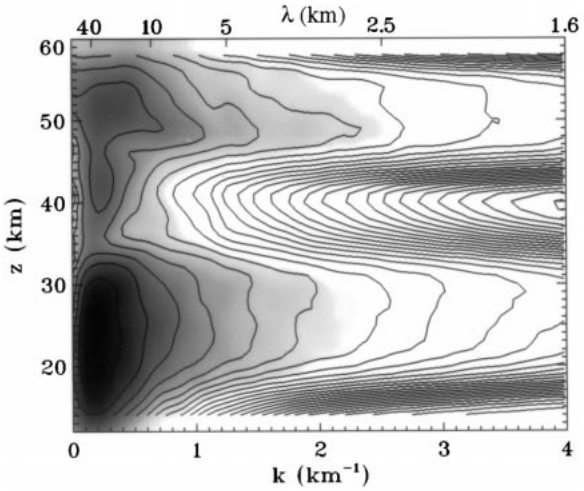

FIG. 5. Time-averaged power spectral density of $\rho^{1/2}w'$ as a function of horizontal wavenumber k (or horizontal wavelength λ) and altitude z. Contours represent the logarithm of power spectral density with an interval of 0.5. The units of spectral energy density are J m^{-3}. Dark shading depicts regions of large power.

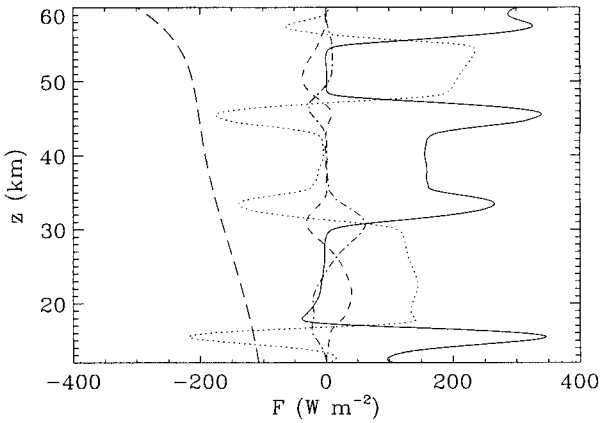

FIG. 6. Time-averaged heat fluxes for the mean wind shear case as a function of altitude. Plotted are the convective heat flux F_c (dot), eddy diffusion heat flux F_e (solid), kinetic energy flux F_k (dash), pressure energy flux F_p (dash–dot), and solar heat flux F_q (long dash).

lengths of 25–30 km compared to 10–15 km in the shear-free case).

Heat transfer in the cloud region is altered by the presence of mean wind shear. Figure 6 shows time-averaged heat fluxes where F_c is the convective heat flux, F_e is the eddy diffusion heat flux, F_k is the kinetic energy flux, F_p is the energy flux associated with pressure fluctuations, and F_q is the solar heat flux. These quantities are formally defined in P1. The cloud-level convection layer is characterized by positive convective heat flux F_c with negative kinetic energy flux F_k caused by strong, narrow downwellings. The magnitudes of F_c and F_k in the cloud-level convection layer are similar to the magnitudes of convective and kinetic energy fluxes in the shear-free case (cf. P1, Fig. 8). However, heat transfer in the cloud-level penetrative and entrainment regions is significantly different between the two cases. Cloud-level penetration into the underlying stable layer, represented by negative F_c, is stronger and deeper in the case with mean wind shear (Fig. 6). Average convective penetration extends down to roughly 41-km altitude, roughly 2 km deeper than in the shear-free case. Furthermore, the pressure energy flux F_p is larger in magnitude in the penetrative region with mean wind shear, suggesting that compressional heating due to penetration is more intense. Entrainment of overlying stable air from 56- to 60-km altitude (negative F_c) is also stronger in the presence of mean wind shear. Convective entrainment in the overlying stable layer is limited in extent by the boundary at 60-km altitude.

In the lower atmosphere, the presence of mean wind shear significantly modifies the partitioning of heat transfer. The dominant modes of heat transfer in the lower convection layer are still convective heat flux F_c and solar heat flux F_q (Fig. 6). However, the roles of F_k and F_p in the lower convection layer differ dramatically between the two cases. In the shear-free case (P1, Fig. 8), F_k is directed downward throughout the layer due to the dominance of cold, narrow downwellings, and F_p is directed upward near the bottom of the layer due to strong pressure fluctuations driving diffuse upflows. In contrast, the kinetic energy flux in the mean wind shear case is positive in the lower part of the layer and negative in the upper part of the layer (Fig. 6). This indicates that upflows transport kinetic energy near the bottom, while downdrafts dominate near the top (if upflows and downflows equally transport kinetic energy at a given altitude, F_k is zero at that altitude). Likewise, the pressure energy flux F_p in the lower convection layer is negative below 24-km altitude and positive above this altitude with magnitudes considerably larger than in the shear-free case. Large positive values of F_p near the top of the convection layer suggest that pressure fluctuations play an important role in driving flows in the overlying stable layer (Hurlburt et al. 1986). Downward penetration is limited by the boundary at 12 km. Entrainment above the lower convection layer (perhaps augmented by upward penetration by strong upflows) is considerably enhanced; average entrainment extends up to roughly 40-km altitude, almost to the bottom of the cloud-level penetrative region. Interaction between the two convection layers is therefore more likely in the presence of mean wind shear due to deeper penetration and entrainment.

The eddy diffusion heat flux F_e is negligible in the convection layers and relatively large in the penetrative, entrainment, and stable regions (Fig. 6). In the stable regions, F_e roughly balances the solar heat flux. As discussed in P1, a different value of eddy diffusion would not alter this result. In penetrative and entrainment regions, the large value of eddy diffusion heat flux compensates downward solar and convective heat fluxes. In other words, convective penetration and entrainment

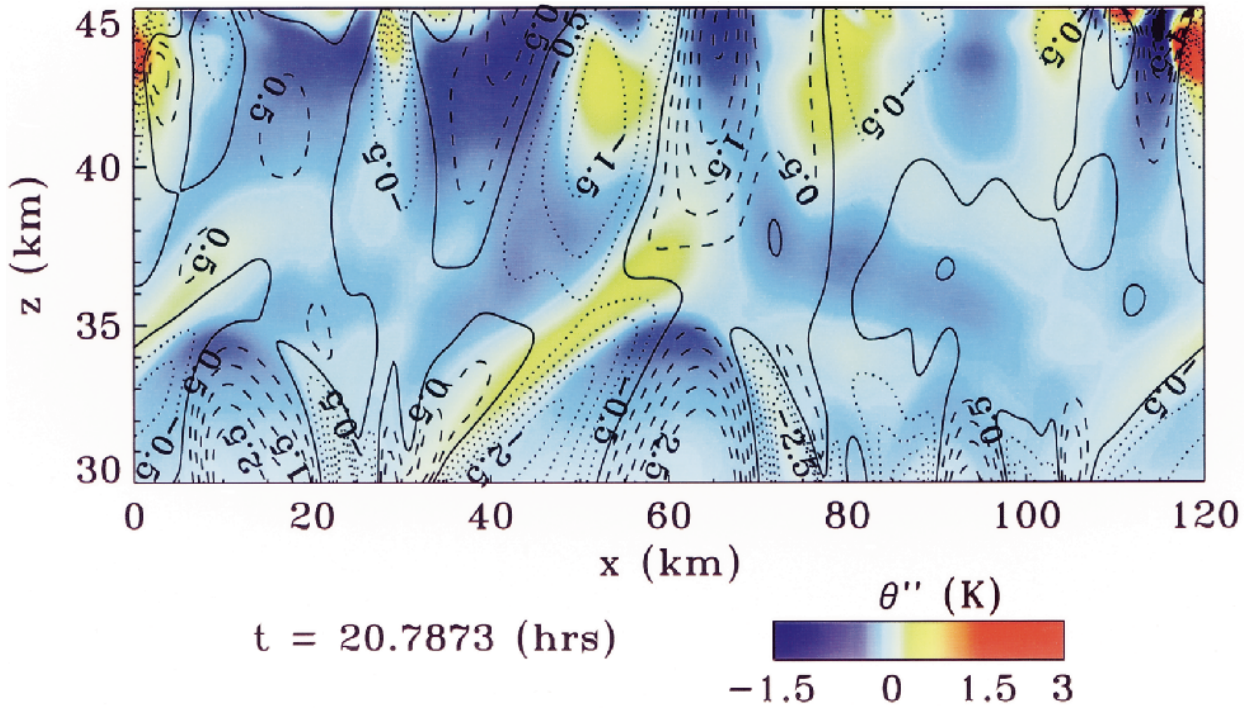

FIG. 7. Residual potential temperature θ'' in the stable layer. Contours of vertical velocity w' are also shown. Positive w' is indicated by dashed lines, negative w' by dotted lines, and zero w' by solid lines. The contour interval is 0.5 m s^{-1}.

produce significant small-scale turbulence above and below the convection layers.

b. Gravity waves

Internal gravity waves occur in the stable layer from 31- to 47-km altitude. Horizontal wavelengths are roughly 25–30 km, comparable in size to both lower-atmosphere convection and cloud-level convection (Fig. 5). Whereas the lower convection layer is largely decoupled from the atmosphere above 34-km altitude in the simulation without mean wind shear; the lower atmosphere in the simulation with a Venus-like mean wind interacts markedly with the overlying stable layer. Figure 7 shows residual potential temperature θ'' and contours of vertical velocity w' in the stable layer from 30- to 45-km altitude. A wave peak in potential temperature located from $x = 35$ km, $z = 32$ km to $x = 65$ km, $z = 38$ km in Fig. 7 is coupled to a downflow (composed of both warm and cool air) in the lower convection layer at roughly $x = 30$ km, $z = 30$ km (see also Fig. 2a). This wave feature is a gravity wave modified by convective entrainment; the peak in potential temperature is roughly correlated with zero vertical velocity (except in the middle portion of the wave feature where convective entrainment is modifying the wave structure), indicating a 90° phase shift characteristic of internal gravity waves. However, convective entrainment is beginning to disrupt the gravity wave. The zero vertical velocity contour in the upper portion of the wave has been disconnected (at roughly $x = 50$ km, $z = 35$ km) from the zero vertical velocity contour in the lower portion of the wave. A second wave feature located at roughly $x = 5$ km, $z = 35$ km exhibits even more clearly the 90° phase shift. This gravity wave has not been modified by convective entrainment but may possibly be generated by lower-atmosphere convection (generation by lower-atmosphere convection is discussed in more detail below). Gravity waves in the stable layer are vertically trapped by the two convection layers. Nevertheless, vertical wave propagation does occur within the stable layer as revealed by lines of constant phase in potential temperature (i.e., peaks or troughs in potential temperature) tilted from the vertical.

Convective entrainment by the lower convection layer is occasionally connected with convective penetration by cloud-level convection. For example, a column of air at roughly $x = 50$ km with negative vertical velocity (albeit with rather small vertical velocities at 35-km altitude) extends from the lower convection layer to the cloud-level penetrative region at 45-km altitude (Fig. 7). This column of negative vertical velocity is transient in nature; it disappears roughly 20 min later as both mean wind shear and horizontally propagating internal gravity waves disconnect the lower portion of the column from the upper portion. Internal gravity waves therefore play a potentially important role in the possible interaction between lower-atmosphere convection and cloud-level convection. Feedback between the two convection layers may be quite strong in the presence of

mean wind shear as evidenced by similar horizontal spatial scales (wavelengths ~30 km) in both convection regions and in the stable layer (Fig. 5). Such interaction between the two convection layers does not occur in the shear-free simulation.

In the case without mean wind shear, internal gravity waves are generated by convection due to convective plumes periodically impinging on the adjacent stable layer and displacing stable air from its equilibrium level. This process is called the mechanical oscillator effect (Fovell et al. 1992). With the addition of mean wind shear, another type of wave generation by convection is introduced. Convective upflows or downflows penetrating the stable layer can act as an obstruction to horizontal air flow. The mean flow is deflected vertically by this convective ''topography,'' and internal gravity waves are generated (Mason and Sykes 1982; Clark et al. 1986). In numerical simulations of gravity wave generation by boundary layer convection in Earth's atmosphere, it was found that boundary layer convection tends to generate gravity waves by the mechanical oscillator mechanism with horizontal wavelengths roughly two to three times smaller than gravity waves forced by the obstacle effect (Clark et al. 1986). The same situation may apply to convective generation of gravity waves on Venus. Both the mechanical oscillator and obstacle wave generating mechanisms are present in the case with mean wind shear; the spectrum of waves that occurs in the stable layer therefore differs from the spectrum of waves in the shear-free case. Gravity waves in the shear-free case are characterized by relatively short horizontal wavelengths of 10–15 km (P1, Fig. 7), while internal gravity waves in the case with mean wind shear exhibit longer wavelengths of 25–30 km (Fig. 5). As discussed in more detail below, the obstacle effect may be the dominant wave generation mechanism of the longer wavelength gravity waves in the mean wind shear simulation.

Regardless of the precise wave generation mechanism, internal gravity waves are likely forced by both cloud-level convection and lower-atmosphere convection in the presence of a Venus-like mean wind. In the simulation without mean wind shear (P1), it was found that cloud-level convection is the primary wave source for gravity waves in the stable layer. Because of stronger entrainment by the lower convection layer and the introduction of the obstacle effect in the simulation with mean wind shear, lower-atmosphere convection significantly contributes to the gravity wave signal in the stable layer. Figure 8 indicates characteristics of internal gravity waves in the stable layer from 31- to 47-km altitude that could be generated by convection. Eastward (westward) wave propagation is in the direction of positive (negative) x and $\langle \rho u'' w'' \rangle$ is the wave vertical flux of horizontal momentum (brackets indicate the horizontal average, and double primes indicate residuals from the horizontal average). When the generation source is located below the wave region, eastward-

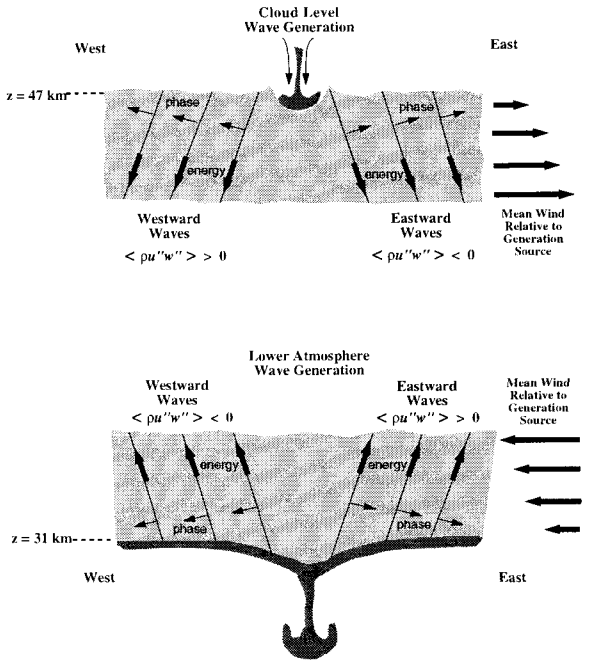

FIG. 8. Properties of internal gravity waves generated by cloud-level convection and lower-atmosphere convection.

(westward-) propagating waves that transfer wave energy upward exhibit positive (negative) correlation between horizontal and vertical velocities; that is, $\langle \rho u'' w'' \rangle > 0$ for eastward-propagating waves and $\langle \rho u'' w'' \rangle < 0$ for westward-propagating waves (Holton 1979). Likewise, eastward- (westward-) propagating waves generated from above that transfer wave energy downward experience negative (positive) $\langle \rho u'' w'' \rangle$. In the simulation with mean wind shear, gravity waves in the stable layer are generally characterized by positive $\langle \rho u'' w'' \rangle$ (see section 3c) and eastward tilting of constant phase with altitude (Fig. 7). Thus, either westward-propagating waves generated by cloud-level convection, eastward-propagating waves generated by lower-atmosphere convection, or both wave types dominate the gravity wave signal in the stable layer. Indeed, animation of residual potential temperature reveals quasi-stationary eastward tilted waves in the lower portion of the stable layer and both eastward- and westward-propagating waves near the top. Quasi-stationary waves are indicative of gravity wave forcing by the obstacle effect (Fovell et al. 1992). Eastward-propagating waves generated by cloud-level convection reach critical levels and are absorbed into the mean flow, leaving westward-propagating waves to dominate the wave signal at the top of the stable layer.

Figure 9 shows 2D spectral energy density of $\rho^{1/2}\omega'$ as a function of Doppler-shifted frequency $\hat{\omega}$ and horizontal wavenumber k in the lower convection layer (24-km altitude), the lower entrainment region (33-km altitude), the stable layer (39-km altitude), the cloud-level penetrative region (45-km altitude), and the cloud-level convection layer (51-km altitude). The density-weighted

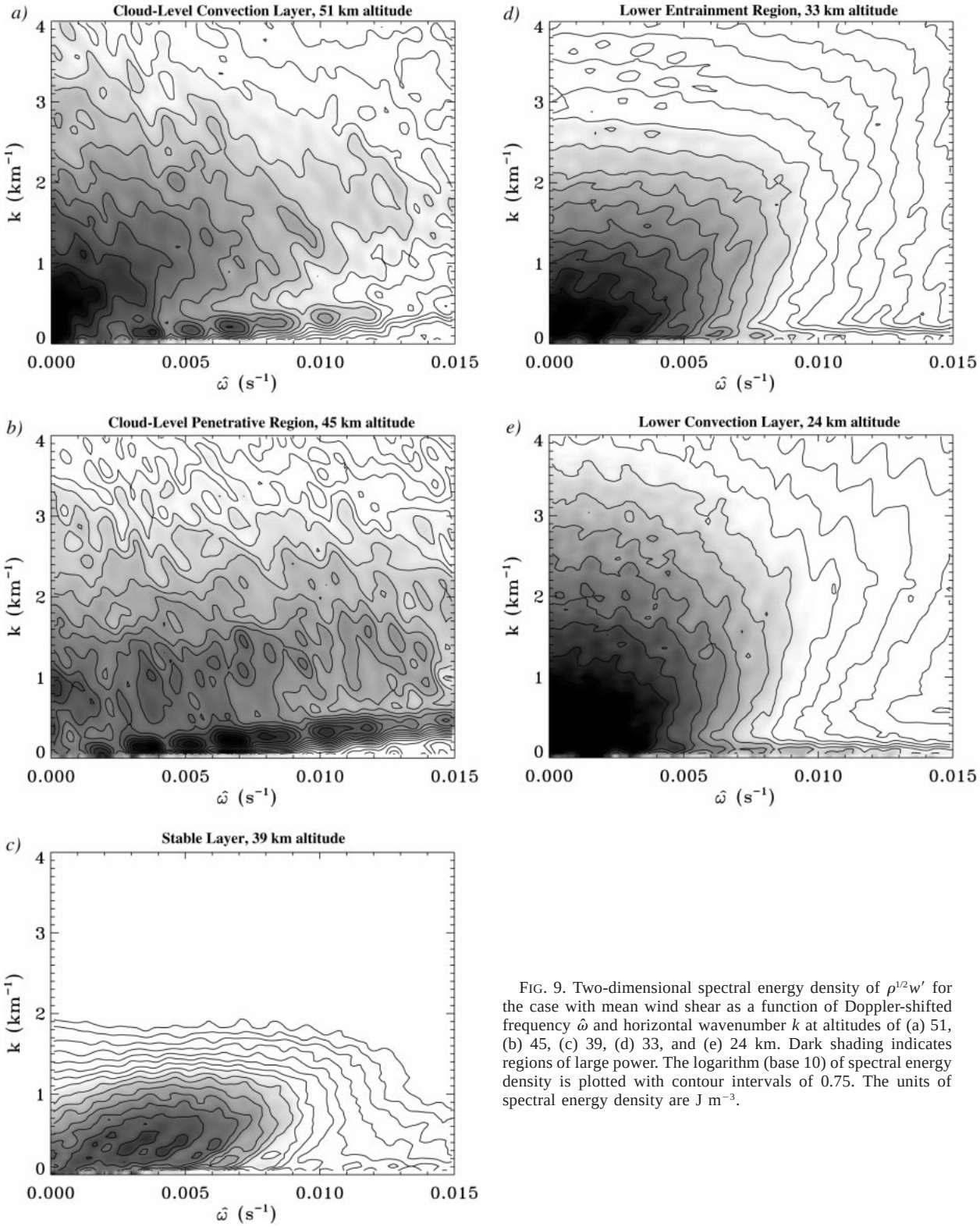

FIG. 9. Two-dimensional spectral energy density of $\rho^{1/2}w'$ for the case with mean wind shear as a function of Doppler-shifted frequency $\hat{\omega}$ and horizontal wavenumber k at altitudes of (a) 51, (b) 45, (c) 39, (d) 33, and (e) 24 km. Dark shading indicates regions of large power. The logarithm (base 10) of spectral energy density is plotted with contour intervals of 0.75. The units of spectral energy density are J m^{-3}.

vertical velocity $\rho^{1/2}\omega'$ was sampled every 100 s at each horizontal grid point at a given altitude from $t = 17.7$ h to $t = 33.1$ h. The Doppler-shifted frequency $\hat{\omega}$ is given by $\hat{\omega} = \omega \pm k\langle u\rangle$, where ω is the frequency, k is the horizontal wavenumber, $\langle u\rangle$ is the horizontally averaged zonal wind, and the plus (minus) sign indicates westward (eastward) wave propagation. Waves propagating in the same direction as the mean wind have Doppler-shifted frequencies less than the absolute frequency ω, while waves propagating in the opposite direction to the mean wind have higher Doppler-shifted frequencies. The Doppler-shifted frequency used in Fig. 9 assumes eastward wave propagation (i.e., $\hat{\omega} = \omega - k\langle u\rangle$). This assumption does not eliminate westward-propagating modes from the spectral analysis. For example, suppose a signal produces a circular feature in ω–k space. Doppler correction of this signal (i.e., application of the linear transformation given above) would transform the circular feature in ω–k space into a linear ''stretched'' feature in $\hat{\omega}$–k space. If this transformation is reversed, the linear feature becomes a circular feature. In essence, Doppler correction collapses linear features in ω–k space to peak like features in $\hat{\omega}$–k space, *as long as the Doppler correction is applied in the right direction.* If the Doppler correction is applied in the opposite direction (i.e., if the wrong sign is used in the Doppler-shifted frequency formula), peak like features will become linear features, and linear features will become more exaggerated linear features. We assume here eastward wave propagation, so eastward waves will collapse into peaklike features in $\hat{\omega}$–k space. However, westward waves will be characterized by stretched linear features in $\hat{\omega}$–k space since the linear transformation is applied in the opposite direction. Thus, the presence or absence of stretched linear features in Fig. 9 documents the primary direction of propagation at that altitude.

Figure 9b shows significant power in a linear ''string-of-pearls'' at low wavenumber over a broad range of Doppler-shifted frequencies. This linear string-of-pearls indicates westward-propagating modes in the cloud-level penetrative region. If $\hat{\omega}$ had been calculated assuming westward propagation, this linear feature would collapse into a tighter range of frequencies and eastward modes would then be characterized by stretched linear features in spectral space. In contrast, the lower penetrative region (Fig. 9d) contains relatively few linear features, suggesting that eastward modes dominate the signal in that region. In the stable layer at 39-km altitude (Fig. 9c), significant power exists in a confined spectral region but with slightly elongated structure, indicating that both eastward- and westward-propagating modes are present.

The 2D spectral analysis shows that when a Venus-like mean wind shear is present, the lower convection layer plays an active role in forcing small-scale atmospheric dynamics in the stable layer. Lower-atmosphere convection exhibits power in a broad range of Doppler-shifted frequencies and wavenumbers (Fig. 9e) similar to (at least to first order) the range of Doppler-shifted frequencies and wavenumbers exhibited by cloud-level convection (Fig. 9a). This result contrasts with the shear-free simulation spectral analysis in which the power signal of lower-atmosphere convection is limited to a narrow range of frequencies (P1, Fig. 12e). Dominant Doppler-shifted frequencies and horizontal wavelengths in the stable layer have counterparts both in the lower entrainment region and in the cloud-level penetrative region. For example, significant power exists at roughly $\hat{\omega} = 3.1 \times 10^{-3}\ \mathrm{s}^{-1}$, $k = 0.30\ \mathrm{km}^{-1}$ (35-min period and 21-km wavelength) in the stable layer (Fig. 9c). In the lower entrainment region at 33-km altitude, significant power also exists at this frequency and wavenumber (Fig. 9d). Both the stable layer and the cloud-level penetrative region exhibit significant power at $\hat{\omega} = 4.8 \times 10^{-3}\ \mathrm{s}^{-1}$ (22-min period) (Figs. 9b,c). Interestingly, power at this frequency also appeared in the shear-free simulation (P1, Fig. 12c), indicating that the mechanical oscillator effect is probably responsible for this signal. The horizontal wavenumber of this signal in the stable layer ($k = 0.4\ \mathrm{km}^{-1}$) is slightly higher than in the penetrative region ($k = 0.2\ \mathrm{km}^{-1}$), suggestive of resonant wave excitation in Venus's atmosphere (Young et al. 1994). Low frequency waves ($\hat{\omega} < 1.0 \times 10^{-3}\ \mathrm{s}^{-1}$) with relatively long wavelengths ($\sim$30–40 km) are also revealed in the 2D spectral analysis at 39-km altitude (Fig. 9c). This low frequency signal represents quasistationary gravity waves generated by the obstacle effect.

The occurrence of nonlinear modes in the stable layer possibly accounts for the broad range of frequencies found in Fig. 9. Coherence, cross-spectrum amplitude, and phase of w' and θ'' at 39-km altitude and $x = 60$ km as a function of Doppler-shifted frequency reveal nonlinear modes with considerable amplitude (Fig. 10). As described in P1, time series of w' and θ'' for linear gravity waves exhibit large coherence and large cross-spectrum amplitude at frequencies less than the Brunt–Väisälä frequency and a phase difference of 90°. In the simulation with mean wind shear, coherence is high at Doppler-shifted frequencies both above and below the Brunt–Väisälä frequency. Large cross-spectrum amplitudes also occur in this frequency range, but the phase difference between w' and θ'', although clustered around 90°, varies from roughly 60° to 120° at these frequencies. This nonlinear signal can be attributed to stronger entrainment by the lower convection layer [convective entrainment by the lower convection layer extends up to roughly 40-km altitude (Fig. 6)]. In addition, significant power at Doppler-shifted frequencies larger than the Brunt–Väisälä frequency indicates high frequency dynamics other than internal gravity waves within the stable layer due to convective penetration and entrainment.

From the 2D spectral analysis, intrinsic phase speeds of wave features at 39-km altitude can be estimated. Doppler-shifted frequencies and wavenumbers with large spectral power indicate intrinsic phase speeds of 4–17 m s^{-1}, comparable to intrinsic phase speeds of 10

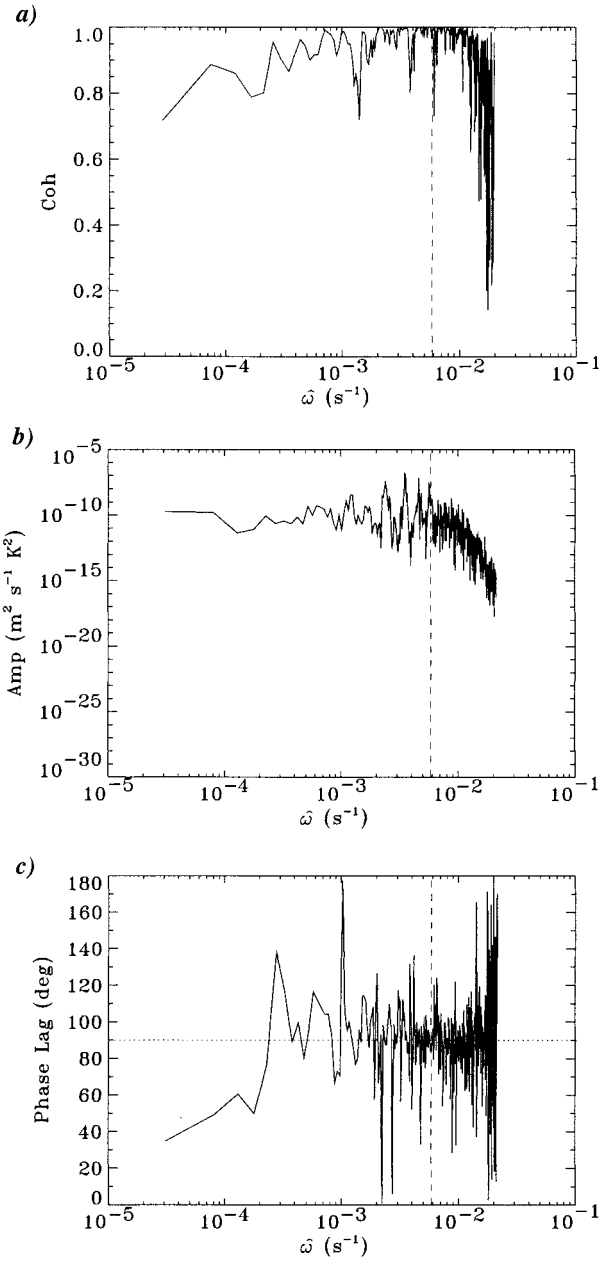

FIG. 10. Coherence (top), cross-spectrum amplitude (middle), and phase (bottom) of w' and θ'' at 39-km altitude and $x = 60$ km as a function of Doppler-shifted angular frequency $\hat{\omega}$. The dashed line is the time-averaged, horizontally averaged Brunt–Väisälä frequency at 39-km altitude. The dotted line in the phase plot marks a phase difference of 90°.

m s^{-1} in the simulation without mean wind shear. Animation of residual potential temperature indicates westward-propagating waves with phase speeds of roughly 15 m s^{-1} in the stable layer above roughly 38-km altitude, suggesting that cloud-level wave generation is responsible for high phase-speed wave features at 39-km altitude.

In the presence of mean wind shear, simulated wave features in the stable layer have potential temperature amplitudes of 0.1–0.8 K (Fig. 2). Furthermore, simulated waves have horizontal velocity amplitudes of 1.1–3.1 m s^{-1} and vertical velocity amplitudes of 0.5–1.9 m s^{-1}. These amplitudes agree well with both Pioneer Venus (Seiff et al. 1980; Counselman et al. 1980) and Magellan observations (Hinson and Jenkins 1995). In addition, vertical wavelengths of simulated waves compare well with observations. Figure 11 shows power spectral density of $\rho^{1/2}w'$ in the stable layer from 31- to 45-km altitude as a function of vertical wavenumber m for both the shear-free and shear cases. Vertical power spectra were taken at every horizontal location and then averaged in space and time. Vertical wavelengths in the simulation with mean wind shear (~7–13 km) are similar to vertical wavelengths in the shear-free simulation and are comparable to Pioneer Venus, Venera 9 and 10, and Magellan observed vertical wavelengths of 5–15 km (Seiff et al. 1980; Counselman et al. 1980; Kerzhanovich and Marov 1983; Hinson and Jenkins 1995). Thus, simulations both with and without a Venus-like mean wind are consistent with observations of wave features in the stable region below the cloud layer.

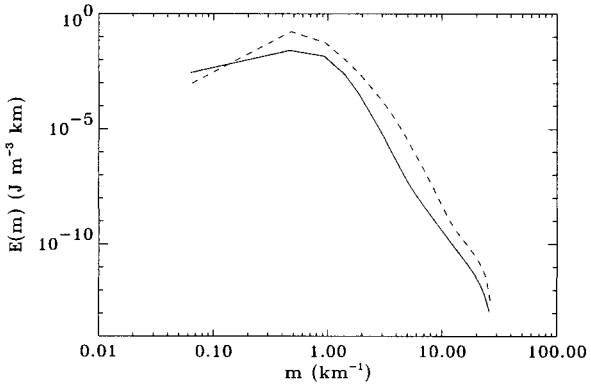

FIG. 11. Time-averaged, horizontally averaged power spectral energy density of $\rho^{1/2}w'$ in the stable layer from 31- to 45-km altitude as a function of vertical wavenumber m for the no mean wind shear case (solid) and the mean wind shear case (dashed).

c. *Convection-mean flow and wave-mean flow interaction*

Both atmospheric convection and convectively generated internal gravity waves can interact with and modify the mean wind. For example, convective parcels may carry horizontal momentum from their original altitude to a new vertical level, mix with environmental air, deposit horizontal momentum at the new altitude, and thus accelerate or decelerate the mean flow (Asai 1970). Similarly, vertically propagating internal gravity waves may reach critical levels where the horizontal phase speed of the wave equals the mean flow velocity. Wave momentum and energy are absorbed at critical levels (Booker and Bretherton 1967; Lindzen 1990). If wave

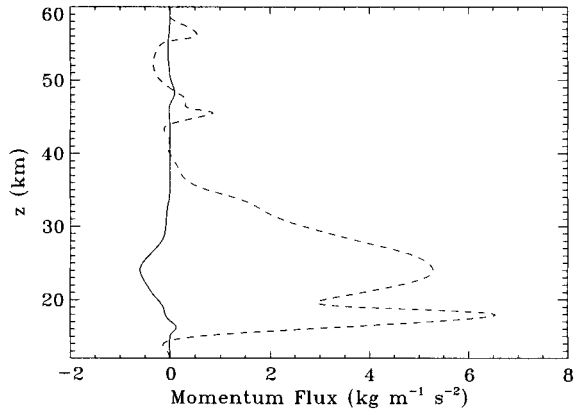

FIG. 12. Time-averaged, horizontally averaged momentum flux $\langle \rho u'' w'' \rangle$ for the shear-free case from $t = 16.6$ h to $t = 32.4$ h (solid) and the mean wind shear case from $t = 25.1$ h to $t = 33.1$ h (dashed).

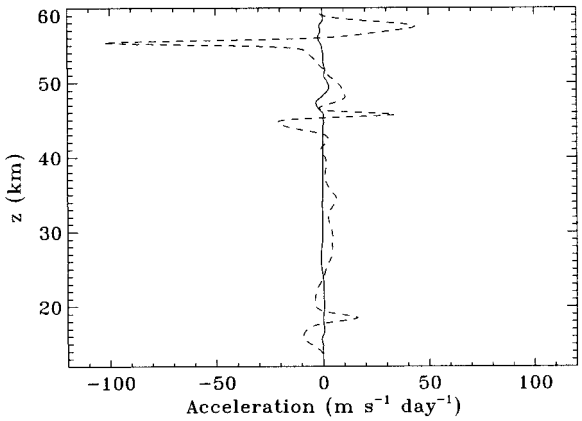

FIG. 13. Time-averaged, eastward acceleration due to momentum flux convergence for the shear-free case from $t = 16.6$ h to $t = 32.4$ h (solid) and the mean wind shear case from $t = 25.1$ h to $t = 33.1$ h (dashed).

amplitudes become sufficiently steep, gravity waves can become convectively unstable and ''break.'' Breaking gravity waves dump their momentum and energy at the altitude of breakdown, and the mean flow can be appreciably modified (Walterscheid and Schubert 1990).

Figure 12 shows the time-averaged, horizontally averaged vertical flux of horizontal momentum $\langle \rho u'' w'' \rangle$ as a function of altitude for both simulations. Momentum flux in the shear-free case is almost negligible, except perhaps in the lower convection layer around 24-km altitude where a negative momentum flux occurs. This negative momentum flux indicates a slight tilt of convective updrafts and downdrafts to the west during a portion of the simulation (P1, Fig. 4). In comparison, the momentum flux is rather substantial in the simulation with mean wind shear (Fig. 12). Lower-atmosphere convection carries westward horizontal momentum downward, indicative of eastward tilting convection cells. Both the lower penetrative region (13–17-km altitude) and the lower entrainment region (31–40-km altitude) also experience downward transport of westward horizontal momentum (positive $\langle \rho u'' w'' \rangle$). For cloud-level convection, on the other hand, $\langle \rho u'' w'' \rangle$ is negative corresponding to upward transport of westward horizontal momentum and westward tilting (to the left) convection cells (Fig. 2). A positive momentum flux exists in the cloud-level penetrative region as penetrative downdrafts carry westward horizontal momentum downward (Fig. 12). Above the cloud-level convection layer, convective entrainment by strong downdrafts also causes a relatively large downward flux of westward horizontal momentum.

Although the magnitude of momentum flux is larger in the lower convection layer than in the cloud-level convection layer, acceleration of the mean flow is substantially greater within the clouds (Fig. 13). Acceleration of the mean flow is caused by convergence of the vertical flux of horizontal momentum; that is, the mean flow is modified where momentum flux changes rapidly. Mean flow acceleration is rather small in the case without mean wind shear but can be quite large in the presence of mean wind shear. The largest acceleration (in magnitude) occurs in the cloud-level entrainment region where downward flux of westward horizontal momentum due to entrainment and upward flux of westward horizontal momentum by convection converge. This convergence of horizontal momentum near the top of the cloud-level convection layer results in a westward increase in the horizontally averaged horizontal wind of 5–8 m s^{-1} by the end of the simulation (Fig. 14). However, large accelerations and decelerations found in the cloud region are only realized near the end of the simulation; much larger modification of the mean wind would have occurred if these accelerations had persisted for longer periods of time. Penetrative regions are characterized by mean flow eastward acceleration just below the convection layer and mean flow eastward deceleration where penetration stalls. Strong eastward accel-

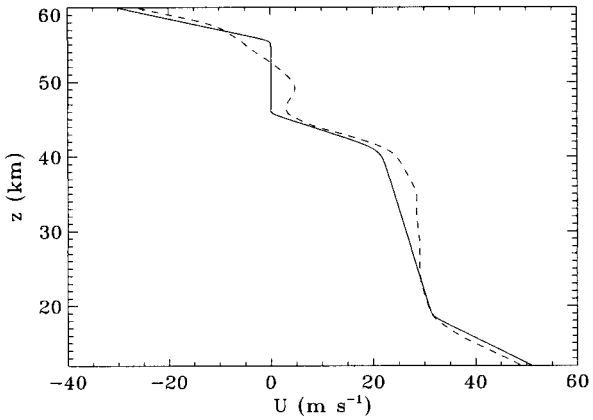

FIG. 14. Horizontally averaged horizontal wind at $t = 33.1$ h (dashed) as a function of altitude. The initial background mean wind is depicted by the solid line.

eration within the cloud-level entrainment region is largely caused by the boundary at 60 km where momentum flux must vanish.

The mean wind is substantially accelerated in the eastward direction from roughly 25- to 41-km altitude (Fig. 14). By the end of the simulation, the horizontally averaged horizontal wind differs from the background state mean wind by as much as 5 m s^{-1}. This modification of the mean wind is likely produced by both convection–mean flow and wave–mean flow interactions. Enhanced convective entrainment in the presence of mean wind shear causes greater mixing near the top of the lower convection layer. Strong vertical mixing tends to smooth wind shear gradients; kinetic energy of the mean flow is converted into kinetic energy of convective motions (Asai 1970). Critical level absorption of eastward-propagating waves generated by cloud-level convection also may account for the mean wind eastward acceleration. Both eastward- and westward-propagating gravity waves are generated by cloud-level convection. Relative to the cloud region, the mean flow in the underlying stable layer is eastward. Eastward waves with intrinsic phase speeds less than roughly 30 m s^{-1} will reach critical levels in the stable layer and become absorbed into the mean flow. The net result of convection–mean flow and wave–mean flow interactions is that the Venus westward superrotation is *decelerated* below the clouds. This result suggests that mechanisms that help maintain the westward superrotation in the lower atmosphere must also overcome the influence of convection and convectively generated gravity waves on the mean flow in the stable layer.

Given decelerations of 2–5 m s^{-1} day^{-1} in the stable layer from 30- to 45-km altitude (Fig. 13), the westward superrotation in the stable layer would spin down in roughly 1–3 weeks. However, deceleration present in the 33-h simulation may not continue for 1–3 weeks. As the mean flow is modified by critical level absorption, old critical levels are destroyed and new critical levels are created. If phase speeds of convectively generated gravity waves do not match new mean wind speeds, critical level absorption will cease and deceleration of the mean flow will halt.

Wave breaking is not observed in the stable layer, although it may occur in the cloud-level penetrative region. Penetrative convection is a highly nonlinear process involving plume head compression, large vertical displacement of stable air, generation of nonlinear ''interfacial'' waves, and generation of linear internal gravity waves (Baker et al. 1998, 2000). Furthermore, temporal and spatial scales vary dramatically within the penetrative region (Fig. 9b). Wave breaking could contribute to the broad range of frequencies and wavenumbers found in the penetrative region. Indeed, Leroy and Ingersoll (1995) found that most convectively generated gravity waves in the stable layer above the cloud-level convection layer experience ''breaking upon emission'' and do not propagate above 57-km altitude. The boundary at 60-km altitude prohibits us from addressing gravity wave generation in the stable layer above the cloud-level convection layer. However, breaking upon emission could also occur in the penetrative region below the cloud-level convection layer. It is difficult to distinguish between breaking waves in the penetrative region and turbulence induced by penetrative plumes. Regardless, nonlinear penetrative dynamics produces rapid small-scale mixing in the region and may be responsible for turbulence observed at 45-km altitude by radio occultation experiments (Woo et al. 1982).

4. Summary and discussion

Two simulations of deep convection and convectively generated gravity waves are performed in this study, one without mean wind shear (Part I) and the other including the Venus westward superrotation (Part II). The calculations span from 12- to 60-km altitude and include two convection layers from 17- to 31-km altitude and from 47- to 56-km altitude, respectively. Internal gravity waves are generated by convection in the stable layer between these two convection layers. In the simulations without mean wind shear, cloud-level penetrative convection is the primary wave generation mechanism. Intrinsic horizontal phase speeds ($\sim$10 m s^{-1}) of gravity waves in the stable layer are comparable to cloud-level convective downdraft velocities ($\sim$9–13 m s^{-1}). The characteristic timescale of lower-atmosphere convection is two to three times longer than cloud-level convection (convective velocities are two to three times smaller in the lower layer), and the lower atmosphere below roughly 34-km altitude is largely decoupled from the atmosphere above. Gravity wave generation occurs through the mechanical oscillator effect in which convective downdrafts impinging on the underlying stable layer induce buoyancy oscillations below. Convectively generated internal gravity waves due to the mechanical oscillator effect have characteristic horizontal wavelengths of $\sim$10–15 km and dominant periods of 18–25 min. The waves are vertically trapped by the two convection layers with horizontal wave propagation in both directions. Figure 15a schematically depicts the dynamical state of Venus's atmosphere due to convection and gravity waves in the absence of mean wind shear.

In contrast, lower-atmosphere convection is more active in the simulation with mean wind shear (Fig. 15b). Although the convective overturning time in the lower convection layer is still much longer than in the cloud-level convection layer (roughly 11 and 2 h, respectively), convective entrainment by lower-atmosphere convection is much stronger and produces more rapid, small-scale motions. The presence of mean wind shear introduces a second wave generation mechanism due to convection: the obstacle effect, in which convective plumes deflect the mean flow vertically. Gravity waves generated by the obstacle effect are characterized by

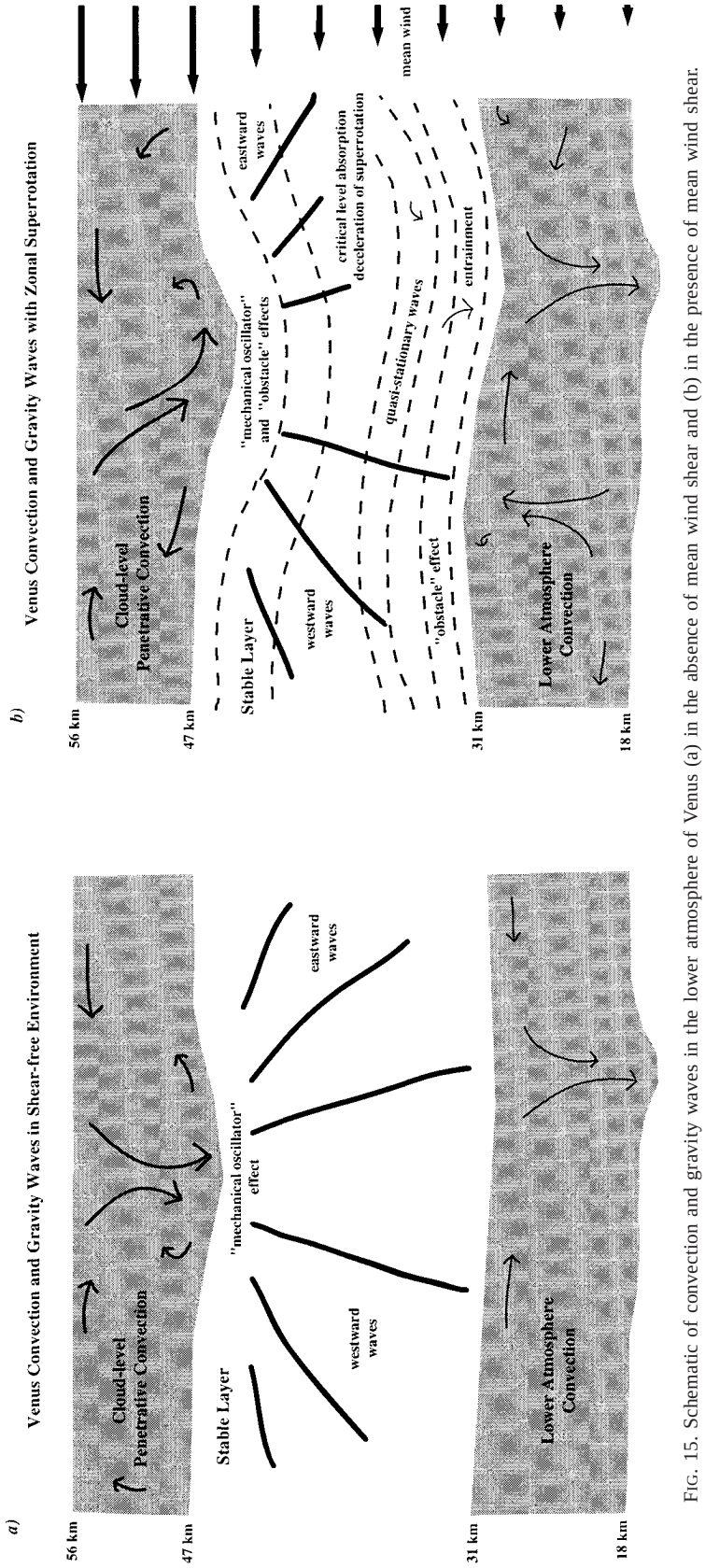

FIG. 15. Schematic of convection and gravity waves in the lower atmosphere of Venus (a) in the absence of mean wind shear and (b) in the presence of mean wind shear.

relatively low frequencies and horizontal wavelengths comparable to the horizontal wavelength of convection (Clark et al. 1986; Fovell et al. 1992). In the simulation with a Venus-like mean wind, quasistationary waves (with respect to the lower convection layer) occur in the lower part of the stable layer from roughly 31- to 41-km altitude, indicative of wave forcing by lower convection layer ''topography.'' Above 37-km altitude, both eastward- and westward-propagating waves are present. These waves are generated by cloud-level convection through both the mechanical oscillator effect and the obstacle effect. Eastward-propagating waves forced by cloud-level convection reach critical levels and are absorbed by the mean wind. The mean wind in the stable layer is modified by as much as 5 m s^{-1} by strong convective entrainment and critical level absorption.

Interaction between the two convection layers is more probable in the presence of mean wind shear. Because of strong convective entrainment above the lower convection layer, the lower atmosphere is no longer decoupled from the atmosphere above. Average cloud-level penetration extends down to roughly 41-km altitude, while lower-atmosphere entrainment reaches up to 40-km altitude. The potential coupling of lower atmosphere dynamics to cloud-level dynamics has significant implications for transporting volatiles from the lower atmosphere to the cloud tops. For example, the amount of sulfur dioxide within the clouds declined dramatically during the Pioneer Venus mission. Episodic volcanism may be responsible for the enhanced concentration of sulfur dioxide initially detected by Pioneer Venus (Esposito 1984). It is unlikely that volcanic plumes could extend over five pressure scale heights and reach the cloud tops at 65-km altitude unimpeded. However, for volcanic plumes reaching the lower-atmosphere convection layer (the bottom of the lower convection layer is only about 1.3 pressure scale heights above the surface), lower-atmospheric convection in the presence of strong mean wind shear could help transport sulfur dioxide up to roughly 40-km altitude. Turbulent mixing induced by cloud-level penetrative convection would then distribute the newly released sulfur dioxide within the cloud layer.

Strong interaction between the two convection layers has also been proposed to explain the large horizontal scales (~200–1000 km) of cellular features in the subsolar region observed at the cloud tops (Baker and Schubert 1992). Convection cells in the simulations reported here do not achieve large horizontal scales. However, strong communication between the two convection regions may be beginning to occur in the simulation with mean wind shear as evidenced by similar horizontal scales (wavelengths ~30 km) in both convection regions and in the stable layer between them. If penetration and entrainment were more intense [as is potentially the case for subsolar convection with smaller values of eddy diffusivity (Baker et al. 1999)], interaction between the two convection regions would be stronger and broader cells might possibly develop.

The mean wind is significantly modified by convection–mean flow interaction and critical level absorption of internal gravity waves generated by cloud-level convection. Indeed, the Venus westward superrotation is decelerated in the stable layer below the cloud region. The average deceleration within this layer is roughly 2–5 m s^{-1} day^{-1}, comparable in magnitude to equatorial mean zonal wind accelerations *above* the Venus clouds caused by thermal tides (Newman and Leovy 1992) and to zonal forcing of the quasi-biennial oscillation in Earth's equatorial stratosphere by convectively generated gravity waves (Alexander and Holton 1997). Maintenance of the Venus westward superrotation below the clouds now becomes an increasingly difficult problem. Cloud-level convection continually generates internal gravity waves in the stable layer, and eastward-propagating gravity waves (relative to the cloud region) continually reach critical levels within the stable layer and decelerate the mean wind. Mechanisms that support the Venus westward superrotation below the clouds, such as critical level absorption of internal gravity waves generated near the surface (Hou and Farrell 1987) or Hadley circulations (Gierasch 1975; Del Genio et al. 1993; Del Genio and Zhou 1996), not only must produce zonal winds of 40 m s^{-1} in the stable layer but also must counteract the convection–wave induced deceleration that would halt the superrotation within a few weeks.

Undoubtedly, the presence of mean wind shear dramatically influences convection and convectively generated gravity wave characteristics. In our 2D simulation with mean wind shear, convective rolls are aligned perpendicular to the direction of shear. However, the interaction of convection with mean wind shear in real atmospheres is distinctly a 3D process. The preferred mode in three dimensions consists of longitudinal rolls aligned parallel to the direction of shear (Asai 1970). Internal gravity waves generated by the obstacle effect due to longitudinal rolls may possibly have smaller amplitudes since the mean wind is blowing in the direction with the least variation in convective structure. Furthermore, 3D simulations of gravity waves forced by boundary layer convection in Earth's atmosphere indicate that boundary layer convection is organized in ''varicose'' rolls aligned roughly with the mean wind shear, but internal gravity waves in the overlying stable layer show a more scattered pattern (Hauf and Clark 1989). Regardless of the mode of generation, characteristics of internal gravity waves in three dimensions may differ considerably from those in 2D calculations (Andreassen et al. 1994). Three-dimensional simulations of convectively generated gravity waves are therefore required to better understand the interaction among convection, gravity waves, and large-scale dynamics in Venus's atmosphere.

Acknowledgments. The calculation was performed on the San Diego Supercomputing Center (SDSC) Cray T3E and the UCLA Office of Academic Computing IBM SP2. This work was supported by NASA Planetary Atmospheres Program under Grant NAG5-4117.

REFERENCES

Alexander, M. J., and J. R. Holton, 1997: A model study of zonal forcing in the equatorial stratosphere by convectively induced gravity waves. *J. Atmos. Sci.,* **54,** 408–419.

Andreassen, O., C. E. Wasberg, D. C. Fritts, and J. R. Isler, 1994: Gravity wave breaking in two and three dimensions. 1. Model description and comparison of two-dimensional evolutions. *J. Geophys. Res.,* **99,** 8095–8108.

Asai, T., 1970: Three-dimensional features of thermal convection in a plane Couette flow. *J. Meteor. Soc. Japan,* **48,** 18–29.

Baker, R. D., and G. Schubert, 1992: Cellular convection in the atmosphere of Venus. *Nature,* **355,** 710–712.

——, ——, and P. W. Jones, 1998: Cloud-level penetrative compressible convection in the Venus atmosphere. *J. Atmos. Sci.,* **55,** 3–18.

——, ——, and ——, 1999: High Rayleigh number compressible convection in Venus' atmosphere: Penetration, entrainment, and turbulence. *J. Geophys. Res.,* **104,** 3815–3832.

——, ——, and ——, 2000: Convectively generated internal gravity waves in the lower atmosphere of Venus. Part I: No wind shear. *J. Atmos. Sci.,* **57,** 184–199.

Booker, J. R., and F. B. Bretherton, 1967: The critical layer for internal gravity waves in a shear flow. *J. Fluid Mech.,* **27,** 513–539.

Clark, T. L., T. Hauf, and J. P. Kuettner, 1986: Convectively forced internal gravity waves: Results from two-dimensional numerical experiments. *Quart. J. Roy. Meteor. Soc.,* **112,** 899–925.

Counselman, C. C. I., S. A. Gourevitch, R. W. King, G. B. Loriot, and E. S. Ginsberg, 1980: Zonal and meridional circulation of the lower atmosphere of Venus determined by radio interferometry. *J. Geophys. Res.,* **85,** 8026–8030.

Del Genio, A. D., and W. Zhou, 1996: Simulations of superrotation on slowly rotating planets: Sensitivity to rotation and initial condition. *Icarus,* **120,** 332–343.

——, ——, and T. P. Eichler, 1993: Equatorial superrotation in a slowly rotating GCM—Implications for Titan and Venus. *Icarus,* **101,** 1–17.

Droegemeier, K. K., and R. B. Wilhelmson, 1987: Numerical simulation of thunderstorm outflow dynamics. Part I: Outflow sensitivity experiments and turbulence dynamics. *J. Atmos. Sci.,* **44,** 1180–1210.

Eliassen, A., and E. Palm, 1961: On the transfer of energy in stationary mountain waves. *Geofys. Publ.,* **22,** 1–23.

Esposito, L. W., 1984: Sulfur dioxide: Episodic injection shows evidence for active Venus volcanism. *Science,* **223,** 1072–1074.

Fovell, R., D. Durran, and J. R. Holton, 1992: Numerical simulations of convectively generated stratospheric gravity waves. *J. Atmos. Sci.,* **49,** 1427–1442.

Gierasch, P., 1975: Meridional circulation and the maintenance of the Venus atmospheric rotation. *J. Atmos. Sci.,* **32,** 1038–1044.

——, and Coauthors, 1997: The general circulation of the Venus atmosphere: An assessment. *Venus II,* S. W. Bougher, D. M. Hunten, and R. J. Phillips, Eds., University of Arizona Press, 459–500.

Hauf, T., and T. L. Clark, 1989: Three-dimensional numerical experiments on convectively forced internal gravity waves. *Quart. J. Roy. Meteor. Soc.,* **115,** 309–333.

Hinson, D. P., and J. M. Jenkins, 1995: Magellan radio occultation measurements of atmospheric waves on Venus. *Icarus,* **114,** 310–327.

Holton, J. R., 1979: *An Introduction to Dynamic Meteorology.* 2d ed. Academic Press, 391 pp.

——, and R. S. Lindzen, 1972: An updated theory for the quasi-biennial cycle of the tropical stratosphere. *J. Atmos. Sci.,* **29,** 1076–1080.

Hou, A. Y., and B. F. Farrell, 1987: Superrotation induced by critical-level absorption of gravity waves on Venus: An assessment. *J. Atmos. Sci.,* **44,** 1049–1061.

Hurlburt, N. E., J. Toomre, and J. M. Massaguer, 1986: Nonlinear compressible convection penetrating into stable layers and producing internal gravity waves. *Astrophys. J.,* **311,** 563–577.

Jenkins, J. M., P. G. Steffes, D. P. Hinson, J. D. Twicken, and G. L. Tyler, 1994: Radio occultation studies of the Venus atmosphere with the Magellan spacecraft 2. Results from the October 1991 experiments. *Icarus,* **110,** 79–94.

Kerzhanovich, V. V., and M. Y. Marov, 1983: The atmospheric dynamics of Venus according to Doppler measurements by the Venera entry probes. *Venus,* D. M. Hunten et al., Eds., University of Arizona Press, 766–778.

Knollenburg, R. G., and D. M. Hunten, 1980: The microphysics of the clouds of Venus: Results of the Pioneer Venus particle size spectrometer experiment. *J. Geophys. Res.,* **85,** 8039–8058.

Leroy, S. S., and A. P. Ingersoll, 1995: Convective generation of gravity waves in Venus's atmosphere: Gravity wave spectrum and momentum transport. *J. Atmos. Sci.,* **52,** 3717–3737.

Lindzen, R. S., 1990: *Dynamics in Atmospheric Physics.* Cambridge University Press, 310 pp.

Mason, P. J., and R. I. Sykes, 1982: A two-dimensional numerical study of horizontal roll vortices in an inversion capped boundary layer. *Quart. J. Roy. Meteor. Soc.,* **108,** 801–823.

Newman, M., and C. Leovy, 1992: Maintenance of strong rotational winds in Venus' middle atmosphere by thermal tides. *Science,* **257,** 647–650.

Schubert, G., 1983: General circulation and the dynamical state of the Venus atmosphere. *Venus,* D. M. Hunten et al., Eds. University of Arizona Press, 681–765.

Seiff, A., D. B. Kirk, R. E. Young, R. C. Blanchard, J. T. Findlay, G. M. Kelly, and S. C. Sommer, 1980: Measurements of thermal structure and thermal contrasts in the atmosphere of Venus and related dynamical observations: Results from the four Pioneer Venus probes. *J. Geophys. Res.,* **85,** 7903–7933.

——, R. E. Young, R. Haberle, and H. Houben, 1992: The evidences of waves in the atmospheres of Venus and Mars. *Venus and Mars: Atmospheres, Ionospheres, and Solar Wind Interactions, Geophys. Monogr.,* No. 66, Amer. Geophys. Union, 73–89.

Walterscheid, R. L., and G. Schubert, 1990: Nonlinear evolution of an upward propagating gravity wave: Overturning, convection, transience and turbulence. *J. Atmos. Sci.,* **47,** 101–125.

Woo, R., J. W. Armstrong, and A. J. Kliore, 1982: Small-scale turbulence in the atmosphere of Venus. *Icarus,* **52,** 335–345.

Young, R. E., R. L. Walterscheid, G. Schubert, A. Seiff, V. M. Linkin, and A. N. Lipatov, 1987: Characteristics of gravity waves generated by surface topography on Venus: Comparison with the VEGA balloon results. *J. Atmos. Sci.,* **44,** 2628–2639.

——, ——, ——, L. Pfister, H. Houben, and D. L. Bindschadler, 1994: Characteristics of finite amplitude stationary gravity waves in the atmosphere of Venus. *J. Atmos. Sci.,* **51,** 1857–1875.